A FULLY CONNECTED CHANGE DETECTION METHOD OF SAR IMAGES FUSING ORIGINAL IMAGE FEATURES AND CHANGE DETECTION RESULTS

Zhentao Sun[1], Fuzhou Duan[1 2 *], Hongliang Guan[1 2], Fan Yang[1], Yanhui Wang[1], Wenji Zhao[1]

[1] College of Resources Environment and Tourism, Capital Normal University, 105 West Third Ring North Road, Beijing, China - (2210902158, 5482, 2170902110, 5314, 4973)@cnu.edu.cn

[2] Engineering Research Center of the Ministry of Education of Space Information Technology, 105 West Third Ring North Road, Beijing, China - hlguan@cnu.edu.cn

KEY WORDS: SAR, Change Detection, Full connection, Conditional Random Field Model, Post-processing.

ABSTRACT:

The primary strategy to eliminate the effect of scatter noise in synthetic aperture radar (SAR) imagery is usually through filtering or combining neighborhood information. However, both approaches to reducing noise reduce the detection accuracy of change edges with similar characteristics to scatter noise points. Considering the above problems, this letter proposes a post-processing method that applies a fully connected conditional random field theoretical model to fuse the original image information with the initial change detection results. The method first takes the original image information and the initial change detection results as a priori conditions. Secondly, the global spatial information in the original image and the label values in the initial change detection results are fully considered when detecting the changed and unchanged pixels to establish a fully connected relationship between all the pixels and find the label distribution probability of each pixel under the condition of noise suppression, and finally obtain better change detection results. The experimental results on the real SAR dataset confirm the proposed method's effectiveness, robustness, and efficiency.

1. INTRODUCTION

Change detection is the process of analyzing and identifying change areas from images of different time phases of the same area (Blaschke, 2010). With the development of earth observation technology, Synthetic Aperture Radar (SAR) has become an essential tool for military reconnaissance, forest environment monitoring, disaster estimation, urban change, and crop growth condition monitoring(Tsokas et al., 2022) However, the scattering noise in SAR images makes detecting SAR images more complicated than that of ordinary optical images.

The variation detection process can be seen as the analyzing of two different simultaneous images to obtain a binary image. The variation detection method of SAR images generally consists of three steps: (1) Pre-processing: noise reduction, geometric correction, and alignment. (2) Variance image generation: The log-ratio operator is the most widely used (Bujor et al., 2004). (3) Disparity image analysis: Disparity image analysis is a process of image segmentation, where each image pixel in the disparity image is segmented into two categories: changed and unchanged. Thresholding is one of the most commonly used methods, with OTSU and GTIK being the more classical thresholding methods (Bazi et al., 2005; Sezgin et al., 2004); the level set method (Bazi et al., 2010) and the clustering method (Gong et al., 2017) are also used for disparity image analysis. However, these are methods that use pixels as the most basic unit. These methods are too sensitive to noise and must first use filtering to reduce noise in the original image.However, filtering will change the pixel value of each image pixel in the original image while reducing noise, which is prone to the loss of image edge information. PCAKEANS classifies each reduced vector by performing PCA on the neighborhood of each image pixel and then using fuzzy C-mean clustering (FCM) (Celik, 2009); FLICM classifies each image pixel by fusing the spatial and grey-scale information of the neighborhood image pixels and using FCM (Krinidis et al., 2010). In recent years, with the rise of deep learning in computer vision (Arel et al., 2010; Bengio et al., 2013), training deep models has gradually become a research direction, with convolutional neural networks (Vinholi et al., 2020), deep confidence networks (Liu et al., 2018), stacked self-encoders (Dong et al., 2018), PCA-NET (Gao et al., 2016) and other models are widely used in change detection tasks. The method of training deep models avoids fixed and complex equations and can learn and accumulate knowledge, achieving good results in change detection tasks. While the above approach of combining neighborhood information when classifying a single image pixel avoids the need for filtering and noise reduction, the neighborhood can also cause inaccurate edge segmentation, for example, when the number of accurate dissimilar images in the neighborhood of an image pixel is higher than the number of accurate similar images, the image pixel is prone to misclassification.

In summary, in the change detection task in SAR imagery, existing methods are mainly used to avoid noise interference through filtering or neighborhood. However, whether by filtering or neighborhood processing, one problem that cannot be avoided is that both methods reduce edge detection accuracy while eliminating the effect of noise points. However, this edge information is, in many cases, of great value. Since the raw image is the richest in edge information, this letter proposes a

* Corresponding author

fast post-processing method that incorporates the raw image into the initial change detection results, using a fully connected conditional random field as a medium. The method uses existing methods' initial change detection results to construct a first-order potential function. Then it constructs a second-order potential function from the original image pairs and considers the global spatial information of each image pixel in the original image based on the initial change detection results, establishes a fully connected relationship between all image pixels with feature and label values and encourages image pixels with similar features and similar spatial distances to be assigned the same label, thus yielding better results. The method is robust in suppressing the effects of noise and preserving important edge information.

The letter is organized as follows: Section 2 details the post-processing method flow for applying the fully connected conditional random field theoretical model to fuse raw image information and initial change detection results. Section 3 presents the experimental dataset. Section 4 gives the experimental protocol and results, demonstrating the method's effectiveness, robustness, and efficiency. Conclusions are given in Section 5.

2. METHODOLOGY

Given two SAR images $X_1 = \{x_{ij}^1, 1 \leqslant i \leqslant m, 1 \leqslant j \leqslant n\}$ and $X_2 = \{x_{ij}^2, 1 \leqslant i \leqslant m, 1 \leqslant j \leqslant n\}$ acquired at different times in different regions, both with dimensions $m \times n$, change detection aims to generate a binary change image representing the changes that occurred between the dates of the two images. Applying the change detection method from the literature (Celik, 2009), the detected change is represented by $X^c = \{x_{ij}^c, 1 \leqslant i \leqslant m, 1 \leqslant j \leqslant n\}$. This letter it is using the combined graphs $X=\{x_{ij}=(x_{ij}^1, x_{ij}^2), 1 \leqslant i \leqslant m, 1 \leqslant j \leqslant n\}$ of X_1 and X_2, and the change graph X^c to represent the original image and the initial change detection results, respectively. X_{ij} is a 6-dimensional spectral vector combined with the 3-dimensional spectral vectors corresponding to each image pixel in X_1, X_2, where x_{ij}^c refers to the category of each image pixel in the binary change image and takes the value of 0 or 1, with 0 indicating no change and 1 indicating change, and to differentiate from the method in this letter, expressing X^c as the initial detection result from other methods. The flow of the method in this letter is shown in Figure 1.

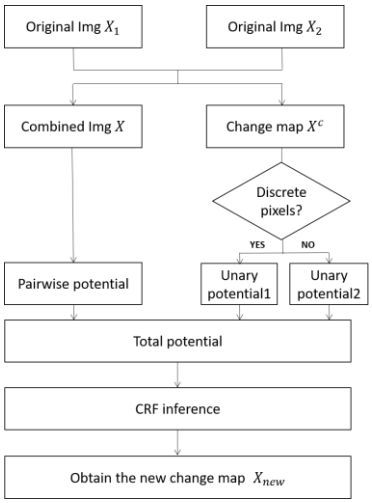

Figure 1. The flowchart of the proposed method

2.1 Fully Connected Conditional Random Field Model

Most of the previous methods derive the change detection result X^c after filtering or neighborhood processing of X. The influence of the original information on the change result needs to be fully considered. In this letter, we will consider combining the original image information X to derive a new change detection image X_{new}, which can be viewed as a random field $Y=\{y_{ij}, i \in (1,m), j \in (1,n)\}$, where the random variable $y_{ij} \in \{0,1\}$ represents whether the image pixel belongs to a changed or unchanged image pixel, respectively. The change detection process can be regarded as the solution of a random distribution satisfying the distribution conditions X and X^c. The original image information and the initial change detection result are used as a priori conditions for the random field Y to construct a conditional random field, and a new change detection image X_{new} can be obtained by solving this conditional random field model.

The probability distribution function corresponding to the fully connected conditional random field $(Y/X, X^c)$ can be defined through the Gibbs distribution in the following form:

$$p(Y/X,X^c)=\frac{1}{Z(X,X^c)}\exp\left(-E(Y/X,X^c)\right) \quad (1)$$

where $Z(X,X^c)$ = the normalisation constants

$E(Y/X,X^c)$ = the potential functions of the conditional random field model

The process of solving for the class of each image pixel in the new change detection image X_{new} can be considered as the process of solving for the maximum posterior probability of the conditional random field $(Y/X, X^c)$, which follows from equation (1):

$$y^*=\text{argmax}P(Y/X,X^c)=\text{argmin}E(Y/X,X^c) \quad (2)$$

I.e., maximizing the probability function $P(Y/X, X^c)$ is equivalent to minimizing the potential function $E(Y/X, X^c)$.

2.2 Fusion of Original Image with Initial Change Detection Result

In order to produce a more accurate new change detection image X_{new}, this letter considers incorporating the original information into the initial change detection result by using the category information of each image pixel in the initial change detection image X^c, the feature similarity and spatial distance information between images in the merged image X to construct two potential functions respectively. The original image information will be incorporated into the initial change detection result by summing the two potential functions:

$$E(Y/X,X^c)=\sum_{ij}\theta_{ij}(y_{ij})+\sum_{ij}\theta_{ij}(y_{ij},y_{ij}') \quad (3)$$

where $\theta_{ij}(y_{ij})$ = The first-order potential function defined by the variogram X^c

$\theta_{ij}(y_{ij},y_{ij}')$ = The second-order potential function defined by the merging image X

By establishing the image pixel potential function of the joint initial detection result and the original data, the fully connected relationship of the random field is established in this letter.

2.2.1 First-order Potential Function: A first-order potential function $\theta_{ij}(y_{ij})$ is constructed using the category information of each image pixel in the initial change detection image X^c as a priori conditions, which is defined by a confidence evaluation of each image pixel's own category in X^c:

$$\theta(y_{ij}) = \begin{cases} -log(p_{ij}) & , y_{ij} = x_{ij}^c \\ -log(1-p_{ij}), & y_{ij} \neq x_{ij}^c \end{cases} \quad (4)$$

where p_{ij} = The probability of y_{ij} belonging to the first category

$1-p_{ij}$ = The probability of y_{ij} belonging to the second category

It follows from equation (4) that the larger p_{ij} is, the smaller the first-order potential function when the random variables y_{ij} and x_{ij}^c take the same value, i.e., the easier it is for the random field to classify the new change detection image X_{new} as being in the same category as the corresponding image pixel (i,j) in the initial change detection image X^c.

The initial change detection image X^c is already highly accurate but only partially free from noise. By dividing the image pixels in the binary change image X^c into two categories and setting different potential functions for each category, the model's ability to suppress noise is increased.

(1) Discrete image pixels
The first category of image pixels is called discrete image pixels, i.e., those that conform to equation (5), as shown in Figure 2:

$$N_{kl}\left[(k,l) \in \Omega_{ij} \cap C(k,l) = C(i,j)\right] <= 2 \quad (5)$$

where Ω_{ij} = The set consisting of all image pixels in the 3×3 neighborhood of point (i,j)

$C(i,j)$ = The category of (i,j) points in the binary change image

$C(k,l)$ = The category of (k,l) points in the X^c image

In the initial change detection image X^c, the image pixel that satisfy equation (5) are usually misclassified due to noise, so setting a minor p_{ij}, i.e., by setting a more significant potential, increases the ability of the model to suppress noise.

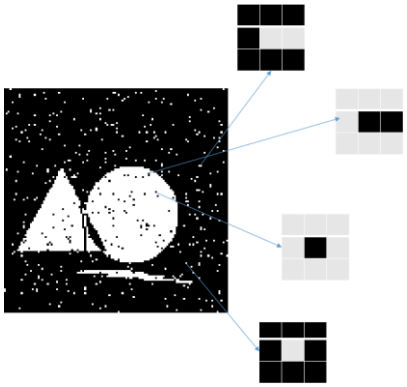

Figure 2. Discrete points

(2) Non-discrete image pixels
The second category of image pixels is called non-discrete image pixels, i.e., image pixels that do not conform to equation (5). Since the X^c derived by the initial change detection method is already very accurate, setting a larger p_{ij} for non-discrete image pixels, the model will tend to trust the classification results of the X^c for image pixel (i,j) more.

After several experimental verifications, the values of p_{ij} for discrete and non-discrete points are set to 0.1 and 0.9, respectively.

2.2.2 Second-order Potential Function: The new change detection image X_{new} obtained from the first-order potential energy function alone is equivalent to the initial change detection image X^c with discrete points suppressed. The edge delineation still needs to be updated. Considering that the original image information has the richest edge information, a second-order potential energy function is defined using spectral feature similarity and the spatial distance of each image pixel from all remaining image pixels in the merged map. Summing the two potential energy functions is used to incorporate the original image information into the initial change detection results, giving the new change detection image X_{new} a more accurate edge region.

In this letter, two Gaussian kernels are used to construct the sum of second-order potential functions to construct the potential function of the original data. The first Gaussian kernel consists of the spectral and spatial information of each image pixel and all other image pixels, while the second Gaussian kernel function is related to the spatial information only, as shown in equation (6):

$$\theta_{ij}(y_{ij}, y'_{ij}) = \mu(y_{ij}, y'_{ij})\left(\omega_1 \exp\left(-\frac{\left\|l_{ij}-l'_{ij}\right\|^2}{2\sigma_\alpha^2} - \frac{\left\|q_{ij}-q'_{ij}\right\|^2}{2\sigma_\beta^2}\right) + \omega_2 \exp\left(-\frac{\left\|l_{ij}-l'_{ij}\right\|^2}{2\sigma_\gamma^2}\right)\right) \quad (6)$$

where y'_{ij} = all random variables in the random field Y except for the random variable y_{ij}

$\mu(y_{ij}, y'_{ij})$ = a label-compatible function to penalize the case where near-neighbor similar image pixels are labeled into different categories; when $y_{ij}=y'_{ij}$, $\mu(y_{ij}, y'_{ij})=1$ when $y_{ij}=y'_{ij}$, and 0 otherwise

ω_1, ω_2 = the corresponding weight coefficients of the first and the second Gaussian kernels

q = a 6-dimensional spectral vector

l = a 2-dimensional image point coordinate vector

σ_α, σ_β, σ_γ = the parameters used to adjust the positional proximity and similarity between the image pixel (i,j) and the rest of the image pixels.

The potential function is mainly used to penalize the inconsistency of annotation results for similar near-neighbor pixels in the new change detection image, which can effectively serve to refine the edge regions. Moreover, one can flexibly adjust the spatial and spectral information proportion between image pixels to achieve different results with such a setting. For

example, when the proportion of ω_1 is higher than ω_2, the model can better refine the edge regions; when the proportion of ω_2 is higher than ω_1, the model can better suppress isolated points.

After the total potential function is obtained, this letter uses the method based on mean-field approximation in the literature (Krähenbühl et al., 2012) to explain the fully connected CRF. The information propagation step in the mean-field approximation can be implemented by Gaussian filtering, accelerating this step and making the whole inference process more efficient.

3 EXPERIMENTS AND ANALYSIS

In order to verify the effectiveness, robustness, and efficiency of the proposed method, two datasets with different regions and sensors were tested in the experiment. The following experiments were also designed in this letter: (1) to verify the effectiveness of this method by setting parameters and analyzing the results; (2) to verify the robustness of this method using multiple datasets and multiple methods; (3) to verify the efficiency of this method by conducting comparison experiments with other post-processing methods for SAR image change detection.

3.1 Introduction to Dataset

3.1.1 Bern Dataset: The first dataset is known as the Bern dataset. The images in this dataset were taken by the European Remote Sensing Satellite SAR sensor around Bern, Switzerland, in April and May 1999. The two SAR images of the first dataset and the reference image of the area of change are shown in Figure 3(a), (b), and (c), with an image size of 301 × 301 pixels. Figure 3(d) shows the log-ratio difference images of the two images, from which it can be seen that they are filled with a large amount of scattered noise.

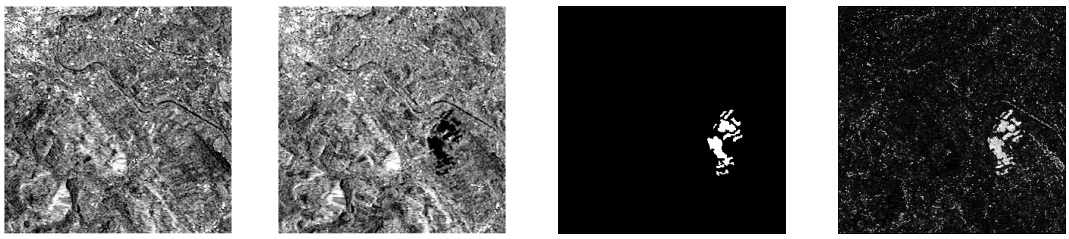

(a) (b) (c) (d)

Figure 3. Multi-temporal images of Bern.(a) Image acquired in April. (b) Image acquired in May. (c) Areas of change. (d) Log-ratio difference image of two images

3.1.2 Ottawa Dataset: The second dataset, known as the Ottawa dataset, consists of two phases of SAR images acquired by Radarsat satellites in the Ottawa area of Canada in May 1997 and August 1997, respectively, both with image sizes of 350 × 290 pixels. The variation in the two phases of images is mainly due to the rise in river levels caused by the rainy season, and Figure 4(d) shows the log-ratio difference between the two images, from which it can be seen that the two images are filled with a large amount of scattered noise.

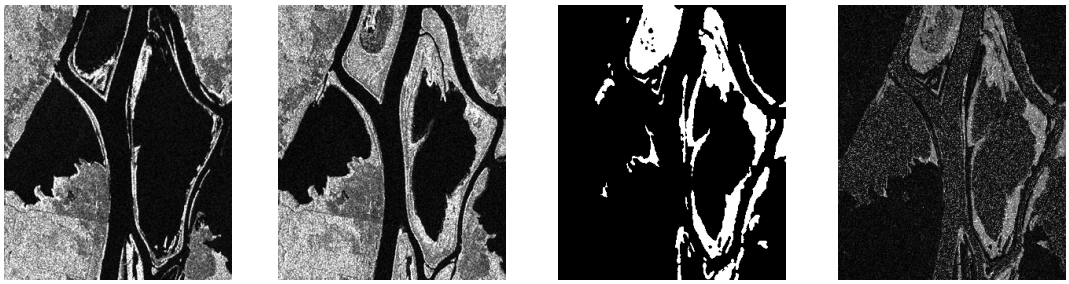

(a) (b) (c) (d)

Figure 4. Multi-temporal images of Ottawa.(a)Image acquired in May. (b) Image acquired in August. (c) Areas of change. (d) Log-ratio difference image of two images

3.1.3 Evaluation Indicators: This letter evaluates the performance of change detection methods in both qualitative and quantitative ways, the former being achieved by visual interpretation and the latter by calculating accuracy metrics for each change image, including false alarms (FA), missed detections (MD), overall error (OE), percentage correct classification (PCC), and kappa coefficient (KC), where FA refers to the number of unchanged pixels that were misclassified as change, MD refers to the number of undetected changed pixels. OE equals FA+MD, i.e., the number of all misclassified pixels. PCC refers to the number of all correctly classified pixels divided by the total number of pixels multiplied by 100%, and the kappa factor is calculated as:

$$\text{Kappa} = \frac{\text{PCC-PRE}}{\text{1-PRE}} \tag{7}$$

where PRE is shown in equation (8):

$$\text{PRE} = \frac{(TP+FP)\cdot(TP+FN)}{(TP+TN+FP+FN)^2} + \frac{(TN+FN)\cdot(TN+FP)}{(TP+TN+FP+FN)^2} \tag{8}$$

where FP = MD
FN = FA
TP = the number of correctly detected changed pixels
TN = the number of correctly detected unchanged pixels

3.2 Effectiveness Experiments

The first set of experiments was used to demonstrate the effectiveness of the proposed method, using the change detection result from the FCM method and the new change detection result after processing by the method proposed in this letter.

Due to the flexibility of the second-order potential function proposed in this letter, setting different parameters would give the model a different performance. When increasing the weight of the first Gaussian kernel function in the second-order potential function, the model would be better able to fine-tune the edges. When increasing the weight of the second Gaussian kernel function, the model would have a better ability to remove noise. As shown in Figure 5, Figures 5(a), (b) show the detection results of the ground truth, and FCM methods, respectively, Figures 5(c), (d) show the new change detection results in different parameters set by the proposed method in this letter, respectively, and Figures 5(e), (f), (g), (h) show the partially enlarged areas in Figures5 (a), (b), (c), and (d), respectively. The parameters θ_α, θ_β, and θ_γ are fixed at 2, 13, and 80 in both images in Figures 5(c), (d). The values of ω_1 and ω_2 are taken as 7 and 3 in Figure. 5(c), making the first Gaussian kernel function have a higher weighting, and the values of ω_1 and ω_2 are taken as 3 and 7 in Figure 5(d), making the second Gaussian kernel function have a higher weighting. As shown in Figures 5(c), (d), Figure 5(d) eliminates more noise relative to Figure 5(c); as shown in Figures 5(g), (h), Figure 5(h) has finer edges relative to Figure 5(g).

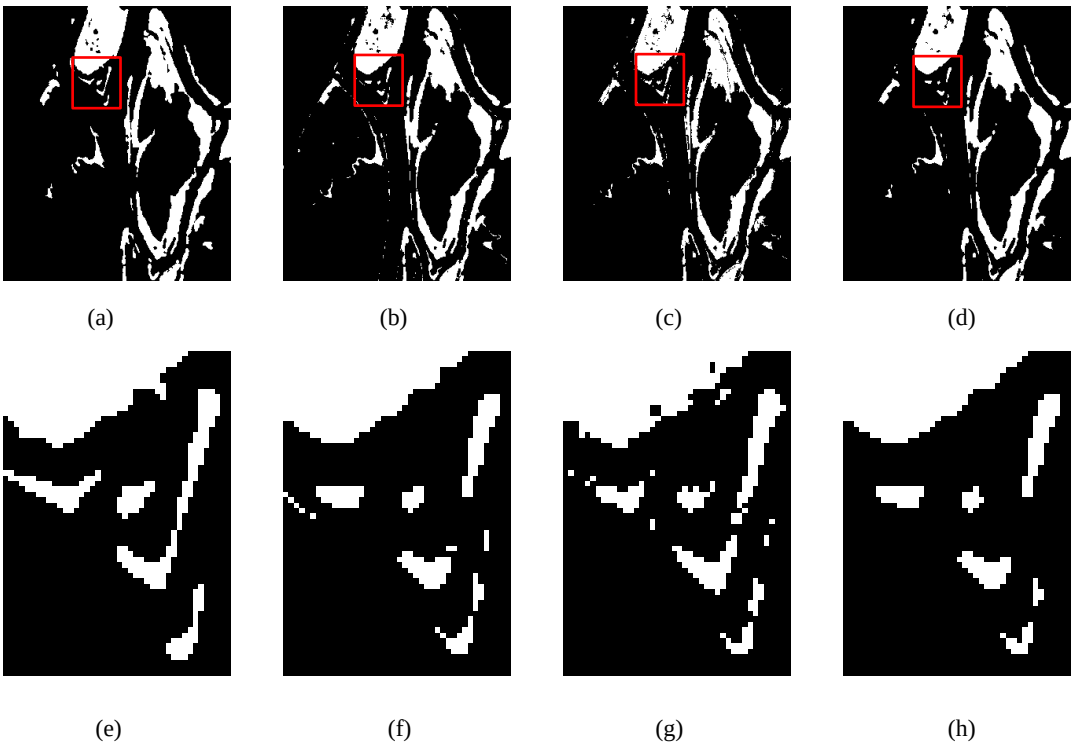

Figure 5. New change-detection images relating to the Ottawa dataset obtained by different Gaussian kernel function parameter settings.(a)Ground-truth. (b) FCM method detection result. (c) Image of the result of the first Gaussian kernel function with high weights. (d) Image of the result of the second Gaussian kernel function with high weights. (e) Part of the enlarged area of Fig. (a). (f) Part of the enlarged area of Fig. (b). (g) Part of the enlarged area of Fig. (g). (h) Part of the enlarged area of Fig. (h).

In order to increase the ability of the model to refine the edges while better-suppressing noise, this letter finally fixed θ_α, θ_β, θ_γ to 2, 13, and 80, and first fixed parameters ω_1, ω_2 to 7 and 3 to eliminate noise and refined the edges of the initial change detection result image. Then, based on the new change detection image obtained, fixed parameters ω_1, ω_2 to 3 and 7 to further eliminate the still residual noise in the new change detection image by choosing different parameters to process the detection results twice respectively, thus achieving the ability to refine the edge regions of the image while suppressing noise. As shown in Figure 6, Figures (a), (b) and (c) is the detection results of ground truth, the FCM method, and the detection result of the FCM method after processing by the proposed method in this letter, respectively. As shown in Figure 6, the edges of the final change

detection result are much finer, and the white speckle noise in the initial change detection result is almost eliminated.

(a) (b) (c)

Figure 6. Image of the results of the second change detection with different parameter settings.(a) Ground-truth. (b) FCM method detection result. (c) Result of proposed method.

Finally, the new detection result obtained by the FCM method processed by the proposed method in this letter is compared with those of PCAKM, MRFFCM, and PCA-NET to demonstrate the effectiveness of the proposed method, and the final results are shown in Table 1. As can be seen from Table 1, the FCM method's detection result is significantly improved by the proposed method in this letter, and the evaluation indexes of the new change detection image are higher than those of PCAKM, MRFFCM, and PCA-NET.

Methods	Result On the Ottawa datasets				
	FA	MD	OE	PCC	Kappa
FCM	1174	1180	2354	0.9768	0.9129
Proposed	449	1318	1767	0.9826	0.9331
PCAKM	949	1570	2519	0.9757	0.9045
MRFFCM	1634	710	2344	0.9769	0.9127
PCA-NET	726	1112	1838	0.9822	0.9306

Table 1. Comparison of experimental results on the effectiveness of the Ottawa dataset

3.3 Robustness Experiments

The second set of experiments was carried out on the Bern and Ottawa datasets, and the change detection results obtained using the threshold method OTSU, the combined neighborhood information method FLICM and the restricted Boltzmann machine method RBM were compared with the new change detection result obtained after processing in this letter to verify the robustness of the proposed method.

3.3.1 Experimental Results for Bern Dataset: The experiment's final results are shown in Figure 8 and Table 3. In Figure 8, figures (a), (b), (c), (d), (e), (f), (g), and (h) show the ground truth, OTSU detection results, FLICM detection results, RBM detection results, OTSU detection results post-processed by the method proposed in this letter, FLICM detection results post-processed by the method proposed in this letter, and RBM detection results post-processed by the method proposed in this letter. As shown in Figures 8(b) and 8(e), the change detection results of the OTSU method still have some white speckle noise and loss of edge information in the images. As shown in Figures 8(c) and 8(f), the change detection results of the FLICM method have a large amount of white speckle noise in the images. After processing by the method proposed in this letter, the number of misclassified pixels is reduced by 10.2%, and the white speckle noise in the images is almost eliminated; as shown in Figures 8(d) and 8(g), the change detection results of the FLICM method have a large amount of white speckle noise in the images. 8(d) and 8(g) show that the change detection result of the RBM method has a small amount of white speckle noise in the image, and after being processed by the method proposed in this letter, the number of misclassified pixels is reduced by 20.3%. The white speckle noise in the image is almost eliminated.

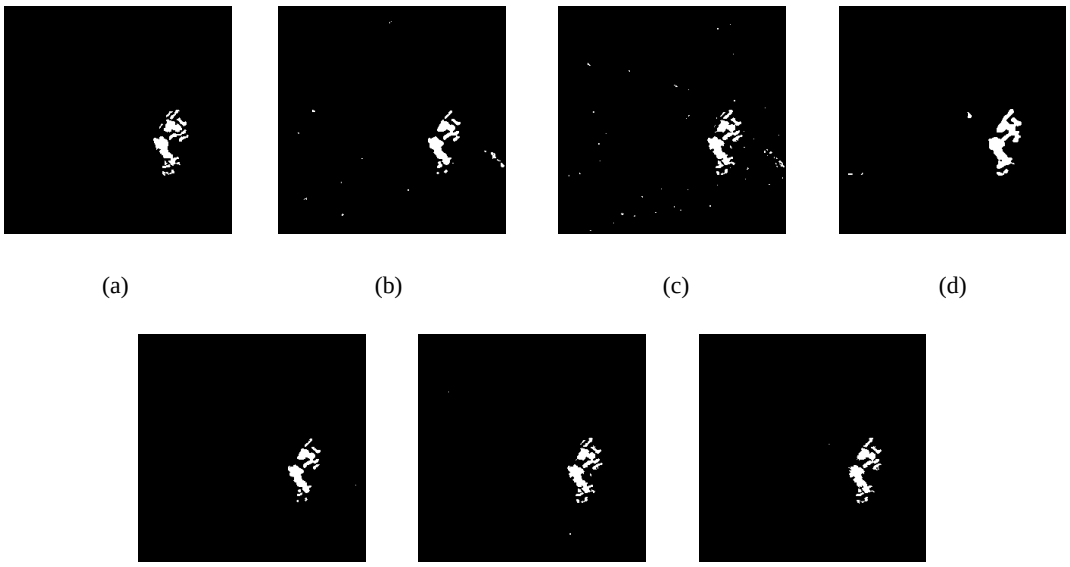

(a) (b) (c) (d)

(e) (f) (g)

Figure 7. Experimental results on the robustness of the Bern dataset. (a)Ground-truth. (b) OSTU experimental result. (c) FLICM experimental result. (d) RBM experimental result. (e) Post-processing result of the OTSU proposed in this letter. (f) Post-processing result of the FLICM proposed in this letter. (g) Post-processing result of the RBM proposed in this letter.

Methods	Result On the Bern datasets				
	FA	MD	OE	PCC	Kappa
OTSU	219	212	431	0.9952	0.8116
Proposed	76	239	315	0.9965	0.8515
FLICM	339	105	444	0.9951	0.8230
Proposed	155	128	283	0.9964	0.8773
RBM	417	123	540	0.9969	0.7896
Proposed	140	184	324	0.9964	0.8552

Table 2. Results of the experimental evaluation of robustness on the Bern dataset

3.3.2 Experimental Results for Ottawa Dataset: The final results of the experiments are shown in Figure 8 and Table 3. In Figure 8 ,Figs. (a), (b), (c), (d), (e), (f), (g), (h) are the ground truth, OTSU detection result, FLICM detection result, RBM detection result, OTSU detection result after post-processing by proposed method in this letter, FLICM detection result after post-processing by proposed method in this letter, RBM detection result after post-processing by proposed method in this letter. As shown in Figs. 8(b) and 8(e), the change detection result of the OTSU method still has some white speckle noise and loss of edge information in the figure. As shown in Fig. 8(c) and 8(f), the change detection result of FLICM method has a large amount of white speckle noise in the figure, and after processing by this method proposed in this letter, the number of misclassified pixels is reduced by 10.2%, and the white speckle noise in the figure is almost completely eliminated; as shown in Fig. 8(d) and 8(g), the change detection result of RBM method has a small amount of white speckle noise in the figure, and after processing by this method proposed in this letter, the number of misclassified pixels is reduced by 20.3%, and the white speckle noise in the figure is almost completely eliminated.

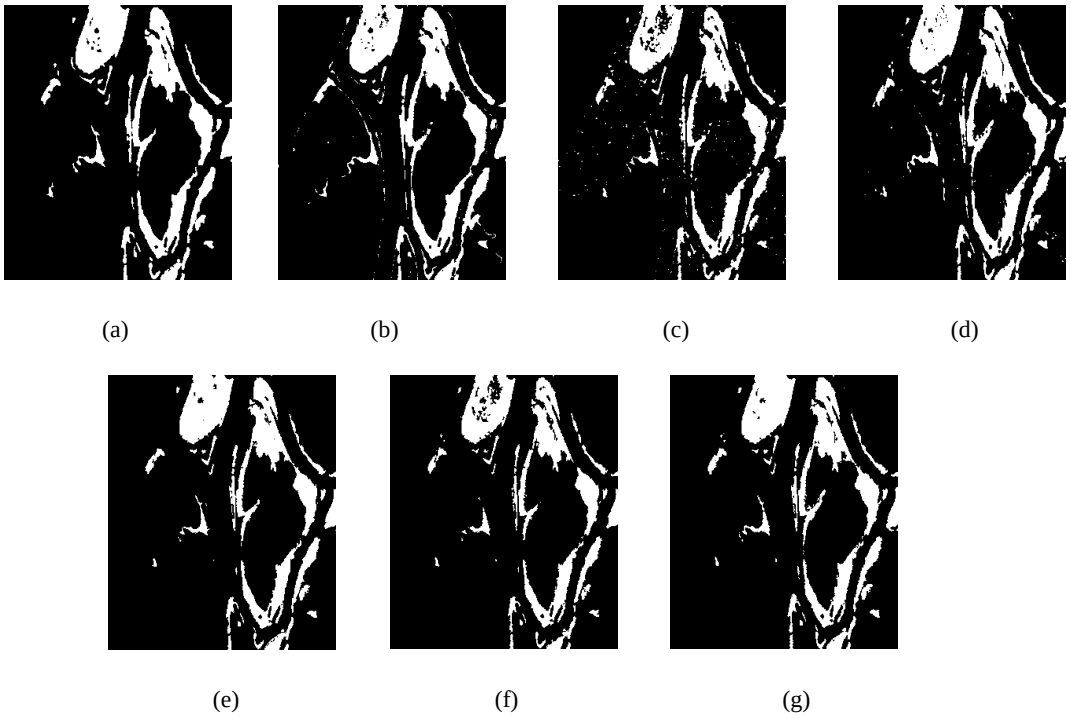

Figure 8. Experimental results on the robustness of the Ottawa dataset. (a)Ground-truth. (b) OSTU experimental result. (c) FLICM experimental result. (d) RBM experimental result. (e) Post-processing result of the OTSU proposed in this letter. (f) Post-processing result of the RBM proposed in this letter.

Methods	Result On the Ottawa datasets				
	FA	MD	OE	PCC	Kappa
OTSU	1260	1090	2350	0.9768	0.9134
Proposed	453	1291	1744	0.9828	0.9341
FLICM	695	2088	2783	0.9726	0.8933
Proposed	180	2346	2526	0.9751	0.9011
RBM	1113	883	1996	0.9803	0.9134
Proposed	624	966	1590	0.9843	0.9406

Table 3. Results of the experimental evaluation of robustness on the Ottawa dataset

3.3.3 Experimental Results Comparing Proposed Method with Other Post-processing Methods: The third set of experiments was carried out on the Bern and Ottawa datasets, using the initial change detection result from the FCM method, followed by post-processing using RBM, MRF, and the proposed method in this letter and comparing the new change detection results to demonstrate the efficiency of the proposed method in this letter. The final results are shown in Figure 9, Figure 10, Table 4, and Table 5. In Figures 9 and 10, Figs. (a), (b), (c), (d), (e) are the ground truth, FCM detection result, and the results obtained by post-processing the RBM, MRF, and the method proposed in this letter on the Bern and Ottawa datasets, respectively.

The experimental results of the Bern dataset: As can be seen from Figure 9, after the detection results of FCM have been processed by the three post-processing methods, RBM eliminates a large number of noise points, but the image segmentation is not detailed enough due to the influence of the neighborhood; MRF only analyses the category relationship between each image pixel and its neighboring image pixels in the label image, which can only play the role of noise reduction and image smoothing, so the method only slightly eliminates the white speckle noise in the image. The method proposed in this letter eliminates almost all the white speckle noise and refines

the edges of the image. As seen from Table 4, the results of this method outperform other methods in all evaluation criteria.

(a) (b) (c) (d) (e)

Figure 9. Bern dataset comparison experimental results.(a)Ground-truth. (b) FCM experimental result. (c) RBM post-processing experimental result. (d) MRF post-processing experimental result. (e) Method proposed in this letter

Methods	Result On the Bern datasets				
	FA	MD	OE	PCC	Kappa
FCM	218	212	430	0.9953	0.8119
RBM	182	233	415	0.9954	0.8140
MRFICM	194	214	408	0.9955	0.8196
Proposed	76	239	315	0.9965	0.8515

Table 4. Results of the comparative experimental evaluation on the Bern dataset

The experimental results for the Ottawa dataset: As can be seen in Figure 10, the FCM result has been processed by the three post-processing methods, with RBM and MRF eliminating a large amount of noise and the proposed method not only eliminating almost all of the noise but also refining the edges of the images. As seen from Table 5, the results of the proposed method outperform other methods in all evaluation indexes.

(a) (b) (c) (d) (e)

Figure 10. Ottawa dataset comparison experimental results.(a)Ground-truth. (b) FCM experimental result. (c) RBM post-processing experimental result. (d) MRF post-processing experimental result. (e) Method proposed in this letter

Methods	Result On the Ottawa datasets				
	FA	MD	OE	PCC	Kappa
FCM	1174	1180	2354	0.9768	0.9129
RBM	590	1433	2023	0.9801	0.9235
MRF	965	1174	2139	0.9789	0.9204
Proposed	449	1318	1767	0.9826	0.9331

Table 5. Results of the comparative experimental evaluation on the Ottawa dataset

Table 6 shows the running times of the three methods, using the dataset Ottawa, size 350 x 290 pixels, platform python 3.5, Intel Core i7-6850K CPU, and NVIDIA GeForce GTX 1080 Ti graphics card. The time taken by the proposed method is significantly less than other methods, which makes it an excellent post-processing method for consideration in practical applications.

Methods	Time(s)
FCM	5
RBM	150
MRFICM	30
Proposed	0.2

Table 6. Comparison of the time taken by different methods

5. CONCLUSIONS

This letter applies the fully connected conditional random field model to establish a fast post-processing method that fuses the original image information with the initial detection results. The initial change detection results are used to construct a first-order potential function. It uses the global spatial information of the original image pair to construct a second-order potential function. The aim is to integrate the original image into the initial change detection result and obtain a new change detection result by summing the two potential functions. Experiments demonstrate that the method can effectively eliminate noise, refine the edges of the detection region and improve the detection accuracy of the initial change detection result and that it only takes 0.2 seconds to process a 350 × 290 pixel SAR image, which is sufficient to demonstrate the effectiveness, robustness, and efficiency of the method. Applying this letter to remote sensing images of different resolutions and proposing new fusion methods are the main directions of our future research.

REFERENCES

Blaschke T., 2010: Object based image analysis for remote sensing. *ISPRS Journal of Photogrammetry and Remote Sensing*, 65(1): 2-16.

Tsokas, A., Rysz, M., Pardalos, P.M., Dipple, K., 2022: SAR data applications in earth observation: An overview. *Expert Systems with Applications*, 2022: 117342.

Bujor, F., Trouvé, E., Valet, L., Nicolas, J.M., Rudant, J.P., 2004: Application of log-cumulants to the detection of spatiotemporal discontinuities in multitemporal SAR images. *IEEE Transactions on Geoscience and Remote Sensing*, 42(10): 2073-2084.

Bazi, Y., Bruzzone, L., Melgani, F., 2005: An unsupervised approach based on the generalized Gaussian model to automatic change detection in multitemporal SAR images. *IEEE Transactions on Geoscience and Remote Sensing*, 43(4): 874-887.

Sezgin, M., Sankur, B., 2004: Survey over image thresholding techniques and quantitative performance evaluation. *Journal of Electronic imaging*, 13(1): 146-168.

Bazi, Y., Melgani, F., Al-Sharari, H.D., 2010: Unsupervised change detection in multispectral remotely sensed imagery with level set methods. *IEEE Trans Geosci Remote Sens*, 48(8):3178 – 3187.

Gong, M.G., Jia, M., Su, L.Z., Wang, S., Jiao L.C., 2014: Detecting changes of the Yellow River Estuary via SAR images based on a local fit-search model and kernel-induced graph cuts. *IEEE International Journal of Remote Sensing*, 35(11-12): 4009-4030.

Celik, T., 2009: Unsupervised change detection in satellite images using principal component analysis and $ k $-means clustering. *IEEE Geoscience and remote sensing letters*, 6(4): 772-776.

Krinidis, S., Chatzis, V., 2010: A robust fuzzy local information C-means clustering algorithm. *IEEE Transactions on image processing*, 19(5): 1328-1337.

Arel, I., Rose, D.C., Karnowski, T.P., 2010: Deep machine learning-a new frontier in artificial intelligence research [research frontier]. *IEEE Computational intelligence magazine*, 5(4): 13-18.

Bengio, Y., Courville, A., Vincent, P., 2013: Representation learning: A review and new perspectives. *IEEE transactions on pattern analysis and machine intelligence*, 35(8): 1798-1828.

Vinholi, J.G., Silva, D., Machado, R., Pettersson, M.I., 2020: CNN-based change detection algorithm for wavelength-resolution SAR images. *IEEE Geoscience and Remote Sensing Letters*, 19: 1-5.

Liu, F., Jiao, L.C., Tang, X., Yang S.Y., Ma, W.P., Hou, B., 2018: Local restricted convolutional neural network for change detection in polarimetric SAR images. *IEEE transactions on neural networks and learning systems*, 30(3): 818-833.

Dong, H.H., Ma, W.P., Wu, Y. Gong, M.G., Jiao, L.C., 2018: Local descriptor learning for change detection in synthetic aperture radar images via convolutional neural networks. *IEEE access*, 7: 15389-15403.

Gao, F., Dong, J.Y., Li, B., Xu, Q.Z., 2016: Automatic Change Detection in Synthetic Aperture Radar Images Based on PCANet. *IEEE Geoscience and Remote Sensing Letters*, 13(12):1792-1796.